Assessment of inflow boundary conditions for compressible turbulent boundary layers

Sheng Xu and M. Pino Martin[a)]

Department of Mechanical and Aerospace Engineering, Princeton University, Princeton, New Jersey 08544

A description of different inflow methodologies for turbulent boundary layers, including validity and limitations, is presented. We show that the use of genuine periodic boundary conditions, in which no alteration of the governing equations is made, results in growing mean flow and decaying turbulence. Premises under which the usage is valid are presented and explained, and comparisons with the extended temporal approach [T. Maeder, N. A. Adams, and L. Kleiser, "Direct simulation of turbulent supersonic boundary layers by an extended temporal approach," J. Fluid Mech. **429**, 187 (2001)] are used to assess the validity. Extending the work by Lund *et al.* [J. Comput. Phys. **140**, 233 (1998)], we propose an inflow generation method for spatial simulations of compressible turbulent boundary layers. The method generates inflow by reintroducing a rescaled downstream flow field to the inlet of a computational domain. The rescaling is based on Morkovin's hypothesis [P. Bradshaw, "Compressible turbulent shear layers," Annu. Rev. Fluid Mech. **9**, 33 (1977)] and generalized temperature–velocity relationships. This method is different from other existing rescaling techniques [S. Stolz and N. A. Adams, "Large-eddy simulation of high-Reynolds-number supersonic boundary layers using the approximate deconvolution model and a rescaling and recycling technique," Phys. Fluids **15**, 2398 (2003); G. Urbin and D. Knight, "Large-eddy simulation of a supersonic boundary layer using an unstructured grid," AIAA J. **39**, 1288 (2001)], in that a more consistent rescaling is employed for the mean and fluctuating thermodynamic variables. The results are compared against the well established van Driest II theory and indicate that the method is efficient and accurate. © *2004 American Institute of Physics.*
[DOI: 10.1063/1.1758218]

I. INTRODUCTION

The simulation of turbulent boundary layers requires streamwise inflow and outflow boundary conditions. The use of a buffer domain[1] or a sponge layer[2,3] in combination with nonreflecting boundary conditions can successfully handle the outflow. The specification of the inflow boundary conditions, however, is more problematic and challenging. A turbulence eddy in a boundary layer has the memory of its upstream history. This fact makes it desirable to specify a realistic time series of turbulence at the simulation inlet. The generation of such a time series of turbulence data results in conflicts between efficiency and accuracy. Creating accurate inflow conditions may require costly independent simulations or forced transition, and a cost-saving but crude inflow generation method may need a long development section behind the inlet for the flow evolution to be realistic. Typical inflow generation techniques can be organized into three categories, as shown in Fig. 1.

The first category consists of the fringe method,[4] the rescaling method,[5] and methods for temporal simulation.[6–8] The inflow in this category comes from the outflow with or without modification. The fringe method distinguishes a fringe region, in which finite extra terms are added to the

governing equations to remove mass and decrease boundary layer thickness, and a useful region for data collection, in which there are no extra terms. In the streamwise direction, the simulation domain is assembled with one useful region and two fringes at its ends and periodic boundary conditions are applied. Thus, the flow that goes out from the downstream end of the data collection region comes into the upstream end after passing through the two fringes. The method results in a spatial simulation and can take into account the streamwise pressure gradient. The rescaling method is based on scaling laws of turbulent boundary layers. The inflow is generated by rescaling the flow field at a downstream station and reintroducing it at the upstream inlet. It can be easily implemented to yield a spatial simulation and works very well with little or no transient near the inlet boundary. In temporal simulations, periodic boundary conditions are used, artificially making the inflow exactly the same as the outflow. A turbulence eddy going out from the outlet comes back into the domain at the inlet without any modifications. To reduce artificial effects, the streamwise size of the domain should be large enough at least to decorrelate turbulence eddies at the inlet and those in the middle between the inlet and the outlet. A genuine temporal simulation solves the original governing equations, while improved temporal simulations add forcing in the governing equations to account for the streamwise inhomogeneity of boundary layers.

The second category involves inflow generation by out-

[a)]Author to whom correspondence should be addressed. Telephone: 609-258-7318; fax: 609-258-1993. Electronic mail: pmartin@princeton.edu
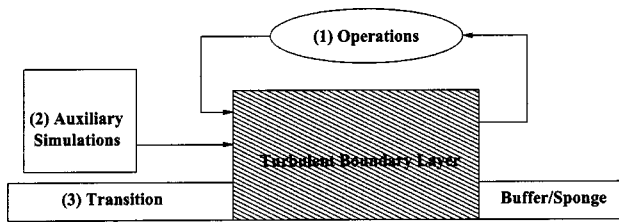
FIG. 1. Schematic showing inflow generation techniques.

side mechanisms, such as an auxiliary simulation and superposition of random fluctuations on desired mean profiles. Li et al.[9] present a method to generate the inflow boundary conditions for large eddy simulations (LES) of turbulent free shear flows. In the method, a time series of instantaneous velocity planes from an auxiliary simulation is recycled repeatedly to provide the inflow. They transform the time signal into a periodic one using a windowing technique. The periodicity induced by the inflow takes 25% of their test domain to die out. Adams[10] used a similar approach to provide the inflow for his direct numerical simulation (DNS) of a turbulent compression ramp. Large-eddy simulation (LES) of supersonic compression-ramps by Rizzeta et al.[11,12] and DNS of turbulent flow over a rectangular trailing edge by Yao et al.[13] also use auxiliary simulations to generate turbulence inflow. The specification of the inflow by superposition of random fluctuations on mean flows is a straightforward procedure. This procedure is successful in the simulations of spatially decaying compressible isotropic turbulence.[14] Other implementations with varying degrees of success include DNS of the spatial laminar-to-turbulent transition[15] and DNS of a backward-facing step.[16] The shortcoming of the method is the requirement of a fairly long development section due to the lack of proper phase information and nonlinear energy transfer. Also, it is very hard to control the skin friction and integral thickness at the end of the development section. Klein et al.[17] develop a method for generating pseudoturbulent inflow. It provides some advantages over the classical approach that uses random fluctuations. The method is based on digital filtering of random data and is able to reproduce a prescribed one-point second order statistics as well as autocorrelation functions.

The last category has the most straightforward approach.[15,18] The computation of the spatially developing turbulent boundary layer starts far upstream, where a laminar profile plus disturbances is set up to allow a transition to turbulence. No time-dependent inflow is required, but the cost is daunting. The approach is generally used to investigate transition itself, see Refs. 19–22.

In the current paper, we present an examination of inflow boundary conditions for compressible turbulent boundary layers. We first discuss and analyze the use of periodic boundary conditions toward temporal simulations. In this regard, we introduce the genuine temporal direct numerical simulation (TDNS) and show the premises under which TDNS can be used to generate turbulent boundary layer data. We then use the extended temporal direct numerical simulation (ETDNS) (Ref. 10) to assess the validity of TDNS. To

relax the conditions that must be satisfied for the validity of TDNS we introduce a new rescaling method that leads to spatial simulations of compressible turbulent boundary layers. Results from the rescaling method are given and also compared to the well-established theoretical predictions.[23] Stolz and Adams[24] and Urbin and Knight[25] implement similar methods. The differences between these methods and the present technique are described in Sec. III.

II. PERIODIC BOUNDARY CONDITIONS

Periodic boundary conditions are widely used in the homogeneous directions of turbulent simulations. The usage is proved to be valid by many numerical experiments, though it may not be well justified physically. The advantages of periodic boundary conditions are apparent. No external inputs are required, Fourier representation is applicable and statistical samples are improved. However, their homogeneity requirement usually limits them to simple geometries, such as rectangular isotropic turbulence boxes, turbulent plane channels, and turbulent pipes.

A flat-plate boundary layer under zero-pressure gradient evolves slowly in the streamwise direction and lacks streamwise homogeneity. If the effect of the streamwise inhomogeneity is neglected, periodic boundary conditions may be applied, leading to a temporal behavior of the boundary layer. The majority of boundary layer transition simulations used temporal approaches and achieved notable success accompanied with limitations, see Ref. 26. In turbulent boundary layer simulations, streamwise periodicity may still be assumed, as we address below.

A. TDNS

The use of genuine periodic boundary conditions in the DNS of a zero-pressure-gradient turbulent boundary layer is to apply them in the streamwise direction, besides the spanwise direction, without any change to the governing equations. As a result, the simulation is temporal instead of spatial and can be referred to as temporal DNS or TDNS. In theory, TDNS leads to nonstationary flow with developing mean and decaying turbulence. Also, the wall-normal displacement in the freestream is prohibited. These aftereffects can be illustrated in different ways. Here, we chose to show the effects in the context of the turbulent kinetic energy.

Taking the simulation domain as a control volume $\mathcal{V}$ and denoting its surface as $\mathcal{S}$, as shown in Fig. 2, we integrate the continuity equation and have the following:

$$\frac{\partial}{\partial t}\int_{\mathcal{V}}\rho\,d\mathcal{V}+\oint_{\mathcal{S}}\rho u_j n_j\,d\mathcal{S}=0, \tag{1}$$

where n_j is the normal vector of the surface $\mathcal{S}$. Starting from the continuity and momentum equations, we can deduce the integral equation for total kinetic energy $K\,(=\frac{1}{2}\rho u_i u_i)$ as

$$\frac{\partial}{\partial t}\int_{\mathcal{V}}K\,d\mathcal{V}+\oint_{\mathcal{S}}(u_j K-u_i\sigma_{ij})n_j\,d\mathcal{S}$$

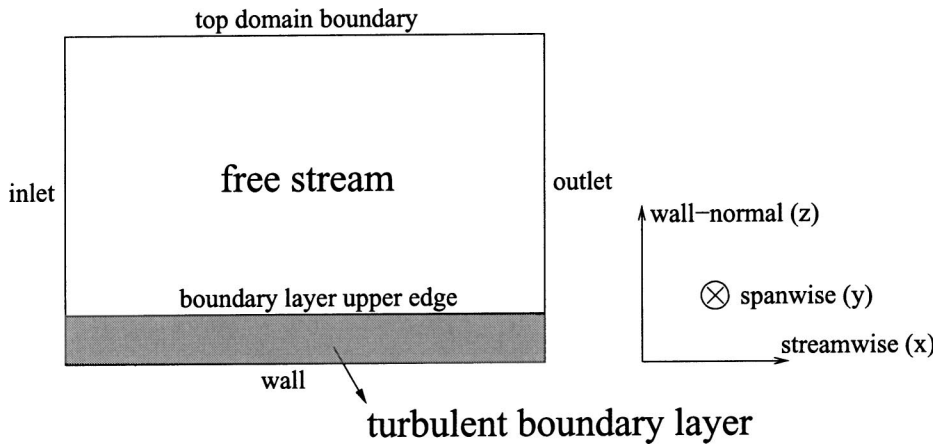$$=\int_{\mathcal{V}}pS_{kk}\,d\mathcal{V}-\int_{\mathcal{V}}\Phi\,d\mathcal{V}, \tag{2}$$

FIG. 2. Schematic of the control volume for analysis in TDNS.

where $\sigma_{ij} = 2\mu S_{ij} - \frac{2}{3}\mu S_{kk}\delta_{ij}$ is the stress tensor, μ is the viscosity, $S_{ij} = \frac{1}{2}(\partial u_i / \partial x_j + \partial u_j / \partial x_i)$ is the rate-of-strain tensor, and Φ is the dissipation. With symmetric boundary conditions at the top boundary of the domain, no-slip and no-penetration boundary conditions at the wall and periodic boundary conditions in the streamwise and spanwise directions, no wall-normal displacement at the top boundary follows Eq. (1) to conserve mass in the domain, and the second term in Eq. (2) thus vanishes for the zero-pressure-gradient boundary layer. Noticing that

$$\int_{\mathcal{V}} p S_{kk} \mathrm{d}\mathcal{V} = \int_{\mathcal{V}} \langle p S_{kk} \rangle \mathrm{d}\mathcal{V}$$

$$= \langle p \rangle \oint_{\mathcal{S}} \langle u_j \rangle n_j \mathrm{d}\mathcal{S} + \int_{\mathcal{V}} \langle p' S'_{kk} \rangle \mathrm{d}\mathcal{V}$$

$$= \int_{\mathcal{V}} \langle p' S'_{kk} \rangle \mathrm{d}\mathcal{V}. \tag{3}$$

We can rewrite Eq. (2) as

$$\frac{\partial}{\partial t} \int_{\mathcal{V}} K \mathrm{d}\mathcal{V} = \int_{\mathcal{V}} \langle p' S'_{kk} \rangle \mathrm{d}\mathcal{V} - \int_{\mathcal{V}} \Phi \mathrm{d}\mathcal{V}, \tag{4}$$

where $\langle \cdot \rangle$ denotes a spatial average in a homogeneous plane and a prime the fluctuation with respect to a spatial mean. With the same boundary conditions, the integral equations resembling Eq. (4) for the mean and turbulent kinetic energy are, respectively,

$$\frac{\partial}{\partial t} \int_{\mathcal{V}} K_m \mathrm{d}\mathcal{V} = - \int_{\mathcal{V}} \mathcal{P} \mathrm{d}\mathcal{V} - \int_{\mathcal{V}} \phi_m \mathrm{d}\mathcal{V}, \tag{5}$$

$$\frac{\partial}{\partial t} \int_{\mathcal{V}} K_t \mathrm{d}\mathcal{V} = \int_{\mathcal{V}} \langle p' S''_{kk} \rangle \mathrm{d}\mathcal{V} + \int_{\mathcal{V}} \mathcal{P} \mathrm{d}\mathcal{V} - \int_{\mathcal{V}} \Phi_t \mathrm{d}\mathcal{V}, \tag{6}$$

where $K_m = \frac{1}{2}\langle \rho \rangle \tilde{u}_i \tilde{u}_i$ is the mean kinetic energy, $K_t = \frac{1}{2}\langle \rho u_i'' u_i'' \rangle$ is the turbulent kinetic energy, $\mathcal{P}$ is turbulence production, Φ_m and Φ_t are the mean and turbulence dissipation, respectively. We use a tilde to denote a mass-averaged mean and a double prime a fluctuation from a mass-averaged mean.

Production $\mathcal{P}$ and dissipation Φ, Φ_m, and Φ_t are all non-negative within the boundary layer. The pressure dilata-tion in Eqs. (4) and (6) represents a transfer mechanism between internal energy and kinetic energy other than dissipation. The DNS data of Maeder *et al.*[6] at Mach 3, 4.5, and 6 and Guarini *et al.*[27] at Mach 2.5 indicate that the pressure dilatation term is negative in the wall vicinity, resulting in a transfer of kinetic to internal energy. Away from the near-wall region, this term assumes a small positive value and it finally approaches zero at the edge of the boundary layer. The contribution of the pressure dilatation to the gain of total and turbulent kinetic energy is negligible compared with the loss due to dissipation Φ and Φ_t and the pressure dilatation itself. The total kinetic energy and the mean kinetic energy in domain $\mathcal{V}$ thus always decrease with time, which results in the developing of the mean streamwise velocity and the thickening of the boundary layer, and leads to a decrease in the turbulence production and the decay of the turbulence.

Nevertheless, in practice TDNS with periodic boundary conditions may still be used to simulate turbulent boundary layer flow at a particular streamwise location. The necessary conditions are that (i) the turbulence can be considered quasisteady, i.e., it adjusts itself to local conditions much faster than the mean profile develops; and (ii) for the purpose of gathering statistics, the sampling time is shorter than the time scale of the mean profile development. A flow that satisfies these conditions evolves slowly and can be viewed as a good approximation of a stationary station of a boundary layer.

The necessity of the second condition is apparent. Otherwise, correct statistics are inhibited as the mean flow changes apparently in a non-self-similar way. The first condition ensures the second one. It is necessary to initialize the flow field to nearly equilibrium for the realization of these conditions. By nearly equilibrium here, we mean that the terms that contribute to the evolution of the turbulent kinetic energy are nearly balanced. If the initial flow field is far away from equilibrium, TDNS may require a long temporal transient process before it settles down to a quasistationary status. Thus, without appropriate initial conditions we could hardly control the skin friction and the boundary thickness at the end of the transient. Martin[28] addresses the procedure for the initialization of compressible turbulence at nearly equilibrium conditions. The practical validity and limitations of TDNS are illustrated in Sec. IV A 1 using simulation data.
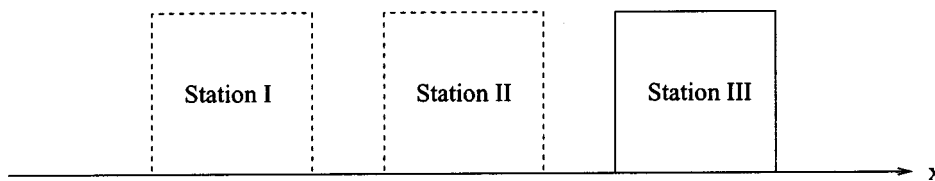
FIG. 3. Schematic of the domains for ETDNS.

B. ETDNS

Stationary mean flow and nondecaying turbulence can be achieved through the addition of forcing to the basic equations. Realizing the fact that both the boundary layer thickness and the energy level of the turbulence vary slowly as functions of the streamwise location, Spalart et al.[7,8] introduced a new wall-normal coordinate and then applied a multiple-scale procedure to approximate the slow streamwise growth of the boundary layer. The final product is a set of small forcing terms that are added to the Navier–Stokes equations. They used the technique and successfully simulated an incompressible turbulent boundary layer at different streamwise stations. Guarini et al.[27] extended the technique to compressible turbulent boundary layer simulations.

Maeder et al.[6] further developed the procedure by Spalart et al.,[7,8] and proposed an extended temporal DNS (ETDNS) approach in which no a priori assumptions about the mean flow are required ETDNS computes a flow at a series of streamwise stations, as seen in Fig. 3, allowing the spatial mean flow evolution to be approximated from its upstream history. When a sufficiently stationary state is reached at a station, the computational box can be marched downstream another spatial step. In ETDNS, the forcing is derived from the spatial evolution history of the mean flow such that the parabolized Navier–Stokes equations are recovered, which is solved locally in time by DNS. Both the mean flow nonparallelism and its interaction with local fluctuations are accounted for in the forcing. For the mathematical derivation of the forcing, we refer to Ref. 6.

There are two remarks worth mentioning for the implementation of ETDNS. One is about the geometric set-up of a simulation. The other regards the forcing at the first station where no upstream history exists, see Fig. 3. The streamwise extent of the domain should be small enough to ensure mod-

est mean flow variation while long enough for turbulence to be decorrelated as in TDNS. In contrast to the simulation by Maeder et al.,[6] our simulation presented later relaxes the former to satisfy the latter. The distance between neighboring stations also has contradictory requirements. It should be long enough to avoid overlap of stations but short enough to achieve the accuracy of the forcing calculation. At the first few stations, the information about the mean flow development from previous stations is either missing or inaccurate, causing a nonphysical spatial transient. We have the same experience as Maeder et al.[6] that the solution can be marched downstream after the temporal transient has settled down appreciably, even before a stationary state is reached.

The advantages of ETDNS are (i) ETDNS achieves stationary flow behavior, i.e., the mean profile keeps and the turbulence sustains; (ii) the marching process allows ETDNS to simulate a series of streamwise stations of a spatially developing boundary layer; and (iii) ETDNS requires no a priori assumptions about the mean flow. But, like TDNS and the approach by Spalart et al.[7,8] ETDNS is a temporal technique in nature and a turbulent eddy does not march from one station to another.

III. RESCALING METHODS

Temporal approaches, such as TDNS and ETDNS, are efficient and useful in turbulent boundary layer simulations. However, they have both physical and numerical limitations. The bridges connecting temporal and spatial simulations through Taylor's hypothesis for supersonic and hypersonic turbulent boundary layers are broken due to their high compressibility, high turbulence intensities, large mean shear, and large viscous effects.[39] Many simulations directly resort to spatial approaches. For example, to numerically investigate the shockwave/turbulent-boundary-layer interaction over a
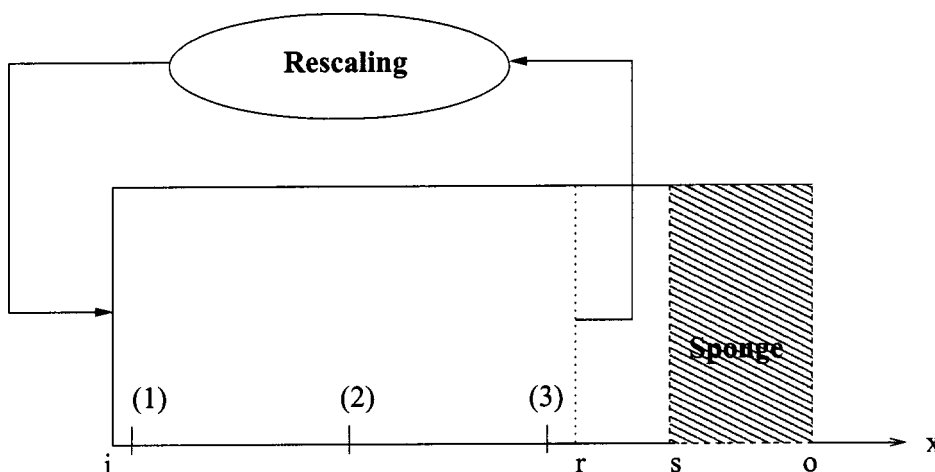

FIG. 4. Schematic of the rescaling methodology.

compression ramp, an inflow–outflow spatial simulation can not be evaded. Still, good inflow generation techniques are desired for this kind of spatial simulations. An auxiliary temporal simulation can be used as an inflow generation device,[5,9,10] however there are constraints regarding computational cost, inflow time periodicity and the control of inflow characteristics. An efficient and accurate way to integrate the inflow generation and the main spatial simulation is highly desirable.

Based on scaling laws of incompressible turbulent boundary layers, Lund et al.[5] proposed a rescaling method to generate turbulent inflow for simulations of spatially developing incompressible turbulent boundary layers. The method rescales the velocity field at a downstream station and then recycles the rescaled velocity field to the inlet, see Fig. 4. Compressible extensions of this method have been developed by Urbin et al.[25] and Stolz and Adams.[24]

The difficulties in the compressible case are that three extra thermodynamic variables, i.e., temperature, density, and pressure, must be rescaled and the velocity field and the temperature field are coupled. The methods by Urbin et al.[25] and Stolz and Adams[24] overcome the difficulties by assuming that all mean and fluctuating thermodynamics variables are scaled in the same way as the wall-normal velocity, which is not justified physically. The scaling of the transformed streamwise velocity holds in the method by Urbin et al. However, it is inconsistent with the scaling of the mean temperature and density. Stolz and Adams assume that the mean density scaled with the freestream value is self-similar in the inner and outer layers. With this assumption their method degenerates the scaling laws for the transformed mean velocity into those of the incompressible case. Both methods[24,25] may work numerically for a zero-pressure-gradient boundary layer when the recycling station is close to the inlet. Our approach is different in that it employs more consistent scalings for all the mean and fluctuating thermodynamic variables. The main assumptions in the method that is presented here are Morkovin's hypothesis[29] and generalized temperature-velocity relationships, which are well justified both theoretically and experimentally.

Morkovin's hypothesis[29] states that the turbulent time scale in a boundary layer is independent of Mach number. Thus, the effects of Mach number are passive to the dynamics of the turbulent boundary layer, and only affect the variation of the fluid properties. The validity of Morkovin's hypothesis is the reason why van Driest's mean-flow scaling is successful. Following Morkovin's scaling, we rescale the velocity field taking into account the density variation across the boundary layer and using the ratio of local density to wall density ($\bar{\rho}/\bar{\rho}_w$, with an overbar denoting averaging in time and w indicating a wall quantity).

Across a boundary layer, the mean pressure is the same as the freestream, and the state equation for perfect gas indicates that the mean density variation is equivalent to the mean temperature variation. Thus, the temperature and the velocity are coupled in the rescaling procedure. We therefore look for a relation between the mean temperature and the mean velocity for the velocity scaling. Walz's equation (also called modified Crocco relation) is an analytical result from

the governing equations and describes very well the relation between mean temperature and mean streamwise velocity for zero-pressure-gradient boundary layers, see Ref. 30. Inspired by the Walz's equation, our method assumes a more general relationship, which may be extended to nonzero-pressure gradient cases. To rescale the temperature fluctuations, we also assume relations between the temperature fluctuations and the velocity fluctuations, including amplitude and phase relations. In this regard, our method is inspired by the strong Reynolds analogy (SRA). However, we should emphasize that the Walz's equation and the SRA are not used in our method. The method that is presented below is more general in this sense.

Due to the presence of multiple length scales in a turbulent boundary layer, we must treat the rescaling process in a piecemeal fashion. To rescale the mean streamwise velocity, we follow Ref. 30 and distinguish the viscous sublayer, the logarithmic region and the law-of-the-wake region in the boundary layer. To rescale the mean wall-normal velocity and turbulence, we divide the boundary layer into the inner layer and outer layer. The implementation of the piecemeal procedure is described in Sec. III D. Hereafter, we denote the streamwise, spanwise and wall-normal coordinates as x, y, z, respectively, with the corresponding velocity components as $u(=U+u')$, $v(=V+v')$ and $w(=W+w')$, where a capital letter represents a mean and a lowercase letter with prime represents a fluctuation. We denote the recycled downstream station as $(\cdot)_r$ and the inlet $(\cdot)_i$.

A. Mean rescaling

For a flat-plate boundary layer, the mean spanwise velocity V is zero due to the spanwise statistical symmetry, and the mean pressure P is equal to the freestream value. Thus, the remaining mean variables to be rescaled are the mean streamwise velocity U, the mean wall-normal velocity W, the mean temperature T, and the mean density $\bar{\rho}$.

1. Mean streamwise velocity

In the viscous sublayer, the viscous shear stress is much larger than the Reynolds shear stress and is assumed equal to the skin friction. Taking the effect of the temperature-dependence of the viscosity, we have

$$\frac{U^s}{u_\tau} = z^+, \tag{7}$$

where $u_\tau = \sqrt{(\nu(\partial U/\partial z))_w}$ is the friction velocity, $z^+ = u_\tau z/\nu_w$ is the wall-normal coordinate in viscous length unit, and U^s is the transformed mean streamwise velocity in the sublayer defined by

$$U^s = \int_0^U \left(\frac{T}{T_w}\right)^n dU, \tag{8}$$

in which T is the mean temperature and the variation of the viscosity with temperature is given by a power law

$$\frac{\mu}{\mu_w} = \left(\frac{T}{T_w}\right)^n. \tag{9}$$

From here on we use the subscripts r and i to refer to the variables at the recycle and inflow conditions, respectively. When $(z^+)_r = (z^+)_i$, i.e.,

$$(z)_r = \frac{(u_\tau)_i}{(u_\tau)_r}\frac{(\nu_w)_r}{(\nu_w)_i}(z)_i = \frac{\omega_{u_\tau}}{\omega_{\nu_w}}(z)_i, \tag{10}$$

in which

$$\omega_{u_\tau} = \frac{(u_\tau)_i}{(u_\tau)_r}, \qquad \omega_{\nu_w} = \frac{(\nu_w)_i}{(\nu_w)_r}, \tag{11}$$

we can compute the transformed velocity U^s at the inlet from

$$(U^s)_i = \omega_{u_\tau}(U^s)_r. \tag{12}$$

In the logarithmic region (also called inertial sublayer), the distance z is assumed to be the only relevant length scale. It can be taken as the mixing length in Prandt's mixing length theory after multiplying a constant k. A logarithmic law is obtained by using either Prandt's mixing length theory or just a scale analysis. The effect of density variation is embodied in the velocity scale. The logarithmic law reads

$$\frac{U^{**}}{u_\tau} = \frac{1}{k}\ln z^+ + C, \tag{13}$$

where C is a constant, U^{**} is the van Driest transformed velocity which is defined by

$$U^{**} = \int_0^U \sqrt{\frac{T_w}{T}}\,dU. \tag{14}$$

In our scaling method for inflow generation, the above form of the law in the logarithmic region is not needed. We only need to use the following self-similar expression:

$$\frac{U^{**}}{u_\tau} = f_{\log}(z^+), \tag{15}$$

where $f_{\log}$ is assumed to be a universal function, see Ref. 30. So when $(z^+)_r = (z^+)_i$, we have

$$(U^{**})_i = \omega_{u_\tau}(U^{**})_r. \tag{16}$$

In the outer layer of a compressible boundary layer, the different similarity law

$$\frac{U_c^{**} - U^{**}}{u_\tau} = f_{\text{wake}}(\eta), \quad \eta = \frac{z}{\Delta}, \tag{17}$$

applies, where f_{wake} is assumed to be independent of streamwise location x, U_e is the freestream velocity, and Δ is an integral reference length taken to be the momentum thickness θ in our rescaling. As the expression indicates, the law is named as the velocity-defect law or the law-of-the-wake. It is well supported by a large number of experiments in zero-pressure-gradient boundary layers. From scaling scheme (17), we can obtain

$$(U^*)_i = \omega_{u_\tau}(U^*)_\tau, $$

$$U^* = U_e^{**} - U^{**} = \int_U^{U_e}\sqrt{\frac{T_w}{T}}\,dU, \tag{18}$$

when $(\eta)_r = (\eta)_i$, i.e., $(z)_r = (z)_i/\omega_\Delta$, where $\omega_\Delta = (\Delta)_i/(\Delta)_r$.

2. Mean wall-normal velocity

From the mean continuity equation, we can approximate W as

$$W = -\frac{1}{\bar{\rho}}\int_0^z \frac{\partial \bar{\rho}U}{\partial x}\,dz. \tag{19}$$

We estimate the order of $\partial\bar{\rho}U/\partial x$ to be $(\bar{\rho}/x)\sqrt{(\bar{\rho}_w/\bar{\rho})}u_\tau$. The order of W then is $(z/x)\sqrt{(\bar{\rho}_w/\bar{\rho})}u_\tau$. So we take $\sqrt{(\bar{\rho}_w/\bar{\rho})}u_\tau$ to be the scale for W. In the inner and the outer layers of the boundary layer, W is assumed to be scaled as

$$\frac{W}{u_\tau}\sqrt{\frac{\bar{\rho}}{\bar{\rho}_w}} = f_{\text{inner}}(z^+), \tag{20}$$

$$\frac{W}{u_\tau}\sqrt{\bar{\rho}/\bar{\rho}_w} = f_{\text{outer}}(\eta), \tag{21}$$

where functions f_{inner} and f_{outer} are assumed to be independent of streamwise location x. The scaling of W above is not justified physically. However, W is very small relative to U and is not a dynamically dominant quantity. Thus, a rigorous treatment of W can be relaxed.

Applied at the recycling station and the inlet, the scaling of W leads to

$$(W)_i = \omega_{u_\tau}\omega_{\rho_w}\sqrt{\frac{(\bar{\rho})_r}{(\bar{\rho})_i}}(W)_r, \tag{22}$$

for $(z^+)_r = (z^+)_i$ in the inner layer and $(\eta)_r = (\eta)_i$ in the outer layer. ω_{ρ_w} is given by

$$\omega_{\rho_w} = \sqrt{\frac{(\bar{\rho}_w)_i}{(\bar{\rho}_w)_r}}. \tag{23}$$

3. Mean temperature

When fluctuations are small, to a first-order approximation, the mean temperature T and the mean density $\bar{\rho}$ are related by the state equation $T = P/R\bar{\rho}$ for perfect gas, where R is the gas constant. Thus, the rescaling of $\bar{\rho}$ follows that of the mean temperature T is known.

The mean temperature appears in the transformed mean streamwise velocities U^s, U^{**}, and U^*. Thus, we need a relationship to decouple the mean streamwise velocity and the mean temperature and to produce the rescaling of T in the process of rescaling U. For a zero-pressure-gradient boundary layer, Walz's equation is such a relation and is given by

$$\frac{T}{T_e} = \frac{T_w}{T_e} + \frac{T_r - T_w}{T_e}\left(\frac{U}{U_e}\right) - r\frac{\gamma-1}{2}M_e^2\left(\frac{U}{U_e}\right)^2, \tag{24}$$

where T_r is the recovery temperature, subscript e indicates a freestream quantity, M_e is the freestream Mach number, γ is the ratio of specific heats, and r is the recovery factor. The recovery temperature T_r and the recovery factor r are related by the definition of the recovery factor as

$$T_r = T_e\left(1 + r\frac{\gamma-1}{2}M_e^2\right). \tag{25}$$

For an adiabatic wall, $T_w = T_r$ and T_r is calculated by Eq. (25). For an isothermal wall, T_w is given and T_r is still calculated by Eq. (25). So Walz's equation tells us that the relation between the mean temperature and the mean streamwise velocity is dependent of the streamwise location only through T_r, or say the recovery factor r. Experimental data indicate that r changes little along a boundary layer. Thus, taking r to be the same at the recycling station and the inlet is a good assumption. In turn, Walz's equation is the same at the two stations. We may generalize the argument by assuming that the relationship between the mean temperature and the mean streamwise velocity is independent of the streamwise location, as expressed by

$$\frac{T}{T_e} = f_{UT}\left(\frac{U}{U_e}\right),\tag{26}$$

where f_{UT} is a function of z^+ in the inner layer and η in the outer layer, and it is not a function of the streamwise location. Note that for a boundary layer under a nonzero pressure gradient, Eq. (26) may not take the same form as Walz's equation. However, the analytic form of this equation is not needed for the rescaling method. We can obtain the relationship numerically at the recycling station and then use interpolation to decouple the mean streamwise velocity and the mean temperature at the inlet. The values of U are obtained from U^s, U^{**}, and U^*. To compute U^s and U^{**}, we start the integration from the wall, where the conditions are known. To compute U^*, we start the integration from the freestream, where the conditions are also known.

B. Turbulence rescaling

The scaling suggested by Morkovin to account for the mean-density variation appears appropriate to at least Mach 5. When the velocity fluctuations are normalized by the velocity scale $\sqrt{(\bar{\rho}_w/\bar{\rho})}u_\tau$, they are in fair agreement with the incompressible data. Applied at the recycling station and the inlet, the scaling of u_i' ($i=1,2,3$ corresponding to u',v',w') by $\sqrt{(\bar{\rho}_w/\bar{\rho})}u_\tau$ leads to

$$(u_i')_i = \omega_{u_\tau}\omega_{\rho_w}\sqrt{\frac{(\bar{\rho})_r}{(\bar{\rho})_i}}(u_i')_r,\tag{27}$$

for $(z^+)_r = (z^+)_i$ in the inner layer and $(\eta)_r = (\eta)_i$ in the outer layer. The difficulty is how to rescale the temperature, density, and pressure fluctuations.

To a first-order approximation, the state equation yields

$$\frac{p'}{P} = \frac{T'}{T} + \frac{\rho'}{\bar{\rho}}.\tag{28}$$

In most cases, p'/P is very small and can be assumed to be negligible, which gives

$$\frac{\rho'}{\bar{\rho}} = -\frac{T'}{T}.\tag{29}$$

This approximation is good for turbulent boundary layers only. Thus, only the temperature fluctuations need to be rescaled. The strong Reynolds analogy (SRA) serves to predict

the relation between the temperature fluctuations and the streamwise velocity fluctuations and is given by

$$\frac{T_{\text{rms}}}{T} = (\gamma-1)M_e^2\frac{u_{\text{rms}}}{U},$$

$$R_{u'T'} = \frac{\overline{u'T'}}{u_{\text{rms}}T_{\text{rms}}} = -1,\tag{30}$$

where T_{rms} and u_{rms} are, respectively, the root mean squared temperature and velocity fluctuations. From the SRA, we can predict T' as

$$T' = -(\gamma-1)M_e^2\frac{u'}{U}T.\tag{31}$$

The SRA is not well supported by simulation data even at low Mach numbers, see Refs. 6 and 27. In contrast, experimental data shows that SRA is well supported for low to moderate Mach numbers, see Refs. 30–34. We can avoid the uncertainty of this assumption in the same way as we deal with the relationship between the mean temperature and the mean streamwise velocity. We assume the following relations which are more general than the SRA,

$$\frac{T_{\text{rms}}}{T} = f_{\text{amp}}\frac{u_{\text{rms}}}{U}, \quad \frac{T'(t)}{T_{\text{rms}}} = c\frac{u'(t+f_{\text{phase}})}{u_{\text{rms}}},\tag{32}$$

where t denotes time, c is equal to $+1$ (or -1), where u' and T' are positively (or negatively) correlated, f_{amp} and f_{phase} are functions of z^+ in the inner layer and η in the outer layer, and they are not functions of the streamwise location. Applying Eq. (32) to the recycling station and the inlet, we can deduce

$$(T'(t))_i = \frac{(u'(t+f_{\text{phase}}))_i}{(u'(t+f_{\text{phase}}))_r}\frac{(U)_r}{(U)_i}\frac{(T)_i}{(T)_r}(T'(t))_r$$

$$= \omega_{u_\tau}\omega_{\rho_w}\sqrt{\frac{(\bar{\rho})_r}{(\bar{\rho})_i}}\frac{(U)_r}{(U)_i}\frac{(T)_i}{(T)_r}(T'(t))_r.\tag{33}$$

Approaching the wall, $(U)_r/(U)_i$ becomes a 0/0 type limit and can be evaluated according to L'Hospital rule. We thus have the following rescaling of the temperature fluctuations at the wall:

$$(T_w'(t))_i = \frac{\omega_{\rho_w}\omega_{\nu_w}}{\omega_{u_\tau}}\sqrt{\frac{(\bar{\rho})_r}{(\bar{\rho})_i}}\frac{(T_w)_i}{(T_w)_r}(T_w'(t))_r.\tag{34}$$

C. Rescaling parameters

To compute rescaling parameters ω's, we need u_τ, ν_w, Δ (in our case, θ) and ρ_w at both the recycling station and the inlet. At the recycling station, these quantities are known. At the inlet, $(\nu_w)_i$ and $(\rho_w)_i$ can be found directly from the mean wall temperature $(T_w)_i$, θ can be specified and u_τ is given as a function of θ using the Karman–Schoenherr equation under van Driest II transformation, see Ref. 23.

D. Implementation

In the rescaling of the mean streamwise velocity, three sublayers are distinguished. In the rescaling of other quanti-
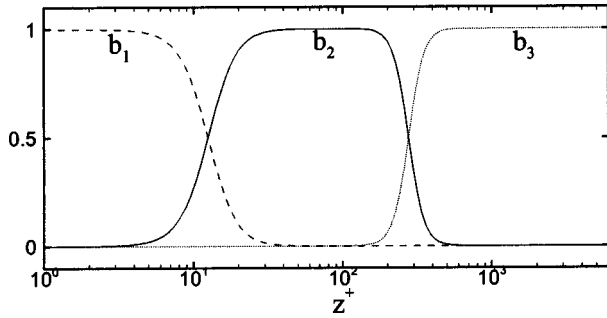
FIG. 5. Weight functions used in the simulation.

ties, the boundary layer is divided into the inner sublayer and the outer sublayer. The composite profile of a quantity over the entire boundary layer is formed by a weighted combination of the profiles for all sublayers. For example, the streamwise velocity is formed as

$$u = \{U_{\text{visc}}b_1(z) + U_{\text{log}}b_2(z) + U_{\text{wake}}b_3(z)\}$$
$$+ \{u'_{\text{inner}}[1 - b_3(z)] + u'_{\text{outer}}b_3(z)\}, \tag{35}$$

where U_{visc}, U_{log}, and U_{wake} represent the mean profiles in the viscous sublayer, the logarithmic region and the wake region respectively, u'_{inner} and u'_{outer} in turn represent the fluctuation profiles in the inner layer and the outer layer, and $b_1(z)$, $b_2(z)$, and $b_3(z)$ are weight functions. The weight functions are constructed from hyperbolic-tangent functions as

$$b_1(k) = \frac{1}{2}\left\{1 - \tanh\left[c_1 \frac{k - k_{m1}}{k_{\text{logs}} - k_{\text{visc}}}\right]\right\}, \tag{36}$$

$$b_2(k) = \frac{1}{2}\left\{\tanh\left[c_1 \frac{k - k_{m1}}{k_{\text{logs}} - k_{\text{visc}}}\right] - \tanh\left[c_{23} \frac{k - k_{m23}}{k_{\text{wake}} - k_{\text{loge}}}\right]\right\}, \tag{37}$$

$$b_3(k) = \frac{1}{2}\left\{1 + \tanh\left[c_{23} \frac{k - k_{m23}}{k_{\text{wake}} - k_{\text{loge}}}\right]\right\}, \tag{38}$$

where k is the wall-normal grid index and equivalent to coordinate z, c_1, and c_{23} are constants to adjust the steepness of the weight functions, k_{visc}, k_{logs}, k_{loge}, and k_{wake} are the wall-normal indexes to distinguish different sublayers, $k_{m1} = (k_{\text{visc}} + k_{\text{logs}})/2$ and $k_{m23} = (k_{\text{loge}} + k_{\text{wake}})/2$. In the simulation presented in the next section, we choose k_{visc}, k_{logs}, k_{loge}, and k_{wake} to correspond to $z^+ = 5$, $z^+ = 30$, $z/\delta = 0.2$, and $z/\delta = 0.5$, respectively. Figure 5 shows the weight functions we used in the simulation. These parameters are chosen based on the simulation conditions during runtime. We find that these parameters are insensitive to the small changes around the initially chosen values.

In the mean scaling, a time average is needed to exclude the starting transient if the flow is initialized with a crude guess. In that case, the following formula is used:

$$U^{(m+1)} = w_1 U^{(m)} + w_2 \langle u^{(m+1)}\rangle_y, \tag{39}$$

where $U^{(m+1)}$ and $U^{(m)}$ are the time-averaged mean at time step $m+1$ and m, respectively, $\langle u^{(m+1)}\rangle_y$ is the average of u in the spanwise direction at time step $m+1$, w_1 and w_2 are

two weights satisfying $w_1 > 0$, $w_2 > 0$, $w_1 \gg w_2$, and $w_1 + w_2 = 1$. Lund et al.[5] let w_1 be $1 - (\Delta t/\tau)$ and w_2 be $\Delta t/\tau$, where Δt is the computational time step and τ the characteristic time scale of the averaging interval. From formula (39), we know

$$U^{(m+1)} = w_1^{m+1} U^{(0)} + w_2(w_1^m \langle u^{(1)}\rangle_y + w_1^{m-1}\langle u^{(2)}\rangle_y$$
$$+ \cdots + \langle u^{(m+1)}\rangle_y). \tag{40}$$

At the beginning of the simulation, because m is small and $w_1 \gg w_2$, $U^{(0)}$ takes a very large fraction of $U^{(m+1)}$, as seen from Eq. (40). Thus, we provide a smooth mean profile from TDNS as $U^{(0)}$ instead of using $\langle u^{(0)}\rangle_y$. We choose w_1 so that when the mean information has propagated from the inlet to the recycling station, m is large enough for $U^{(0)}$ to take almost no effect in $U^{(m+1)}$. After the transient, we increase w_1 to run for N steps in order to stabilize the statistics and then switch to a usual running average, i.e., $w_1 = 1 - [1/(N + m - m_0)]$ and $w_2 = 1/(N + m - m_0)$, where m_0 is the step at which the running average begins. If $U^{(0)}$ is very crude and w_1 is not well attuned, the temporal starting transient can be very long before the right spatial behavior builds up over the boundary layer. If w_1 is too small, a good mean profile $U^{(m+1)}$ can not be achieved due to insufficiency of effective samples for averaging, which leads to wrong scaling and thus wrong boundary layer mean behavior.

If the initial flow field is crude, the rescaling parameters u_τ and θ that are specified at the inlet can largely differ from those calculated at the recycling station initially. The mean streamwise velocity rescaled by the law-of-the-wall thus has a large shift from the one rescaled by the-law-of-the-wake. When the mean profile of the streamwise velocity is formed by the weight functions, there appears an undershoot or overshoot in the profile. We call the start of a simulation with the undershoot or overshoot a jump start. It takes a long time to smooth the undershoot or overshoot and build up the right mean behavior over the whole boundary layer. A trick to avoid this is to let the initial u_τ and θ at the recycling station be the same as those specified at the inlet, and then use the averaging formula (39) to bring their right values at the recycling station slowly in the temporal transient of the simulation. In this way, the simulation starts smoothly. After the initial transient, the averaging formula (39) is discarded and u_τ and θ at the recycling station are calculated directly from the mean profile.

IV. TESTS

In this section, we simulate a supersonic turbulent boundary layer under zero pressure gradient. The perfect gas assumption is used and the specific heats, c_p and c_v, are assumed constants. The dynamic viscosity μ is assumed to obey a power law. We first present the comparisons between TDNS and ETDNS. We check the conditions for the validity of TDNS and point out the improvement over TDNS by ETDNS. We then present the results of a spatial DNS (SDNS) in which the rescaling method is implemented. The numerical results are compared with theoretical ones and those from TDNS and ETDNS.

TABLE I. Parameters for TDNS and ETDNS. $Re_{\theta_0} = \rho_e U_e \theta_0 / \mu_e$. $d_{station}$ is the distance between two neighboring stations in ETDNS. Other symbols take their usual meaning.

Initial flow conditions	M_e	T_e (K)	ρ_e (kg/m³)	$10^3 \delta_0$ (m)	$10^3 \delta_0^*$ (m)	$10^4 \theta_0$ (m)
	4	5000	0.5	6.96	2.87	3.94
	Re_{θ_0}	$u_{\tau 0}$ (m/s)	$10^3 C_{f0}$			
	11363	243	0.96			
Numerical set-up	L_x	L_y	L_z	N_x	N_y	N_z
	$6.10\delta_0$	$1.52\delta_0$	$10.30\delta_0$	384	128	128
	Δx^+	Δy^+	Δz^+	$d_{station}$		
	12.7	9.5	0.11–535	$2L_x$		

We run ETDNS until a stationary station is reached and then take the final flow field as the initial condition to run TDNS and ETDNS. Therefore, the initial flow parameters and numerical set-up are exactly the same. These are given in Table I. To save run time, a coarse spanwise mesh is used for the comparisons between TDNS and ETDNS in Sec. IV A. The initial flow field for SDNS is from a quasistationary TDNS with a fine spanwise mesh. The initial flow parameters and numerical set-up of SDNS are given in Table II. We emphasize that all results in Sec. IV B for the rescaling method are obtained with the fine spanwise mesh. For the resolution and domain assessments, we refer to Ref. 28.

The computational codes for TDNS, ETDNS, and SDNS are essentially the same and are described in Ref. 28. These employ a third-order shock-capturing weighted essentially nonoscillatory (WENO) scheme for the inviscid fluxes, a fourth-order central-finite-difference scheme for viscous fluxes and a second, order accurate data-parallel lower-upper (DPLU) relaxation method for the time advancement. The extra forcing terms for ETDNS are treated explicitly. The marching scheme in ETDNS that is used to approximate derivatives on the slow streamwise scale is a second-order backward finite difference scheme. No-slip and no-penetration conditions for velocity and an adiabatic condition for temperature are used at the lower wall. Symmetric boundary conditions are used at the top domain boundary. In SDNS, we generate the inflow using the rescaling method. The location of the recycling station is given in Table II. We treat the outflow by placing a sponge layer[2,3] before the outflow boundary and applying symmetric boundary conditions at the outflow boundary. In the sponge layer, a vector quantity $\mathbf{Z} = -\sigma(x)(\mathbf{U} - \mathbf{U}_0)$ is added to the right-hand side of the

governing equations, where $\mathbf{U}$ stands for the vector of conservative variables and $\mathbf{U}_0$ a given steady basic flow. Because the recycling station is close to the sponge layer, we let $\mathbf{U}_0$ be the mean flow at the recycling station to reduce the artificial effects from the outflow treatment on the recycling station. Following Israeli *et al.*,[35] the Newtonian cooling function $\sigma(x)$ is chosen to be

$$\sigma(x) = \mathcal{A}(\mathcal{N}+1)(\mathcal{N}+2)\frac{(x-x_s)^{\mathcal{N}}(L_x-x)}{(L_x-x_s)^{\mathcal{N}+2}}, \quad (41)$$

where $\mathcal{A}$ and $\mathcal{N}$ are two adjustable parameters chosen to be 4 and 3, respectively, x_s is the streamwise location where the sponge layer starts given in Table II, and L_x is the streamwise length of the computational domain.

A. Comparisons between TDNS and ETDNS

The purpose of this section is to show that TDNS can be used to generate supersonic turbulent boundary data as long as the specific conditions for its validity, which are listed in the second to last paragraph of Sec. II B, are satisfied. Here, we use the results from ETDNS to test the validity of TDNS.

1. Mean behavior

The theoretical analysis in Sec. II A shows that TDNS leads to nonstationary flow. However, in practice the flow evolves slowly. Thus, if the time interval for averaging is much shorter than the time scale of the flow evolution, then the flow can be considered quasistationary and time averaging can be used to obtain statistics. We verify that the TDNS flow evolution is slow by monitoring the temporal evolution of the friction velocity, momentum thickness and displace-

TABLE II. Parameters for SDNS. x_r is the streamwise location of the recycling station. x_s is the streamwise location where the sponge layer starts.

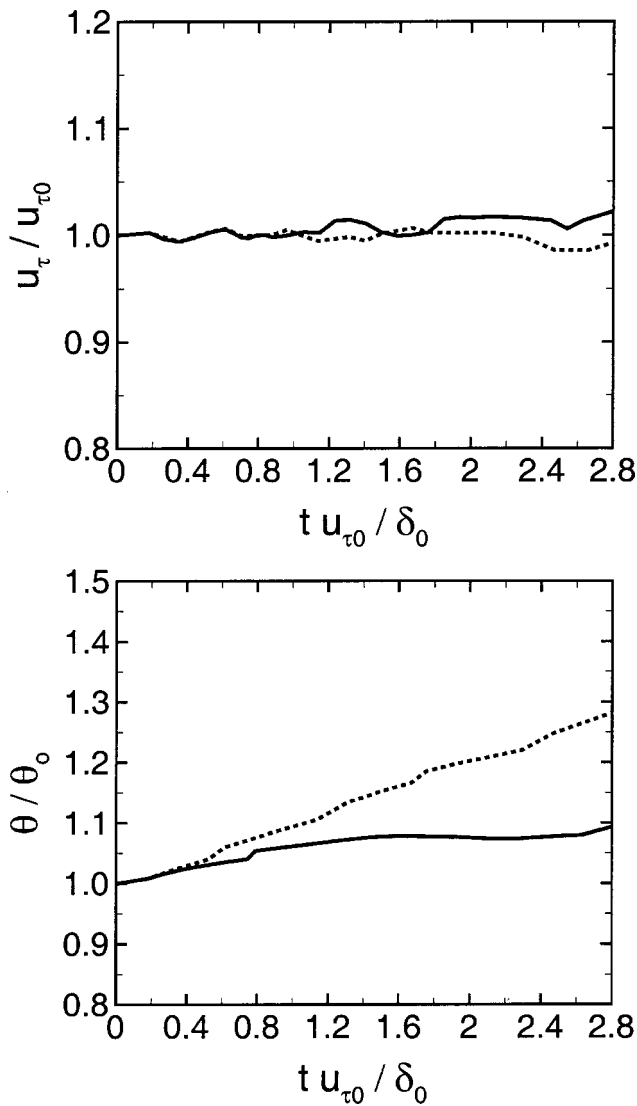| Initial flow conditions	M_e	T_e (K)	ρ_e (kg/m³)	$10^3 \delta_0$ (m)	$10^3 \delta_0^*$ (m)	$10^4 \theta_0$ (m)
	4	5000	0.5	7.44	3.28	4.11
	Re_{θ_0}	$u_{\tau 0}$ (m/s)	$10^3 C_{f0}$			
	11742	255	1.01			
Numerical set-up	L_x	L_y	L_z	N_x	N_y	N_z
	$5.71\delta_0$	$1.43\delta_0$	$9.64\delta_0$	384	256	128
	Δx^+	Δy^+	Δz^+	x_r	x_s	
	12.7	4.8	0.12–565	$4.6\delta_0$	$5.0\delta_0$	

FIG. 6. Temporal evolution of the friction velocity and the momentum thickness for ETDNS (—) and TDNS (---).

Figure 6 shows the time history of friction velocity and momentum thickness for TDNS and ETDNS. In TDNS, the evolution of the skin friction is slow. The long-time temporal evolution of the friction velocity is not obvious in Fig. 6. However, we may expect that u_τ decreases as we continue the simulation much longer. The boundary layer thickening with time in TDNS indicates that the use of genuine periodic boundary conditions does lead to the temporal behavior of the mean flow. In ETDNS, as expected, this temporal evolution is prohibited by the forcing, and the skin friction and the integral thickness evolve little with time.

Estimating the time scale of the boundary layer growth as

$$t_g = \left(\frac{1}{\delta^*} \frac{d\delta^*}{dt} \right)^{-1}, \tag{42}$$

leads to $t_g = 25 \, (\delta_0^*/u_{\tau 0})$ in TDNS for the duration shown in Fig. 6. We find that quasistationary statistics can be gathered in a time-period that is one order of magnitude smaller than
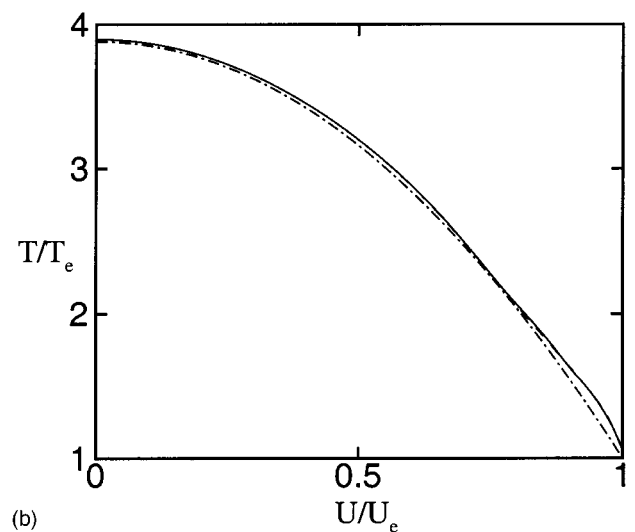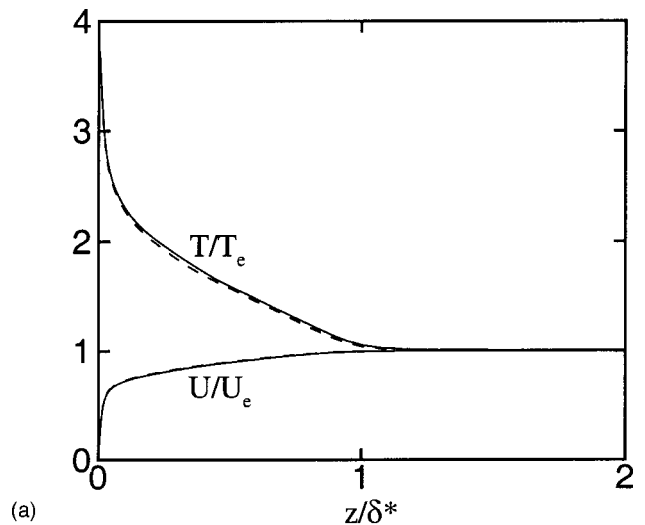
ment thickness and verifying that the change in these quantities is negligible in the time period where the statistics are gathered. In this case, we consider that the variation of these quantities in $3 \delta_0^*/u_{\tau 0}$ is nearly negligible, where δ_0^* and u_τ are the displacement thickness and friction velocity at the beginning of the simulation.
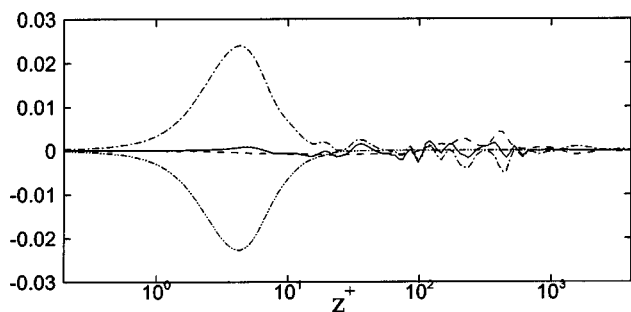
FIG. 7. Mean streamwise momentum balance in ETDNS with $\partial(\rho u)/\partial t$ (—), $\langle f_u \rangle$ (---), $(\partial(\rho u w)/\partial z)$ (−·−), and $\partial(\tau_{xz})/\partial z$ (−·−).

FIG. 8. Mean streamwise velocity and temperature (a) comparison between TDNS and ETDNS; (b) comparison with Walz's equation for $r = 0.9$. ETDNS: —, TDNS: ---, and Walz's equation: −·−.
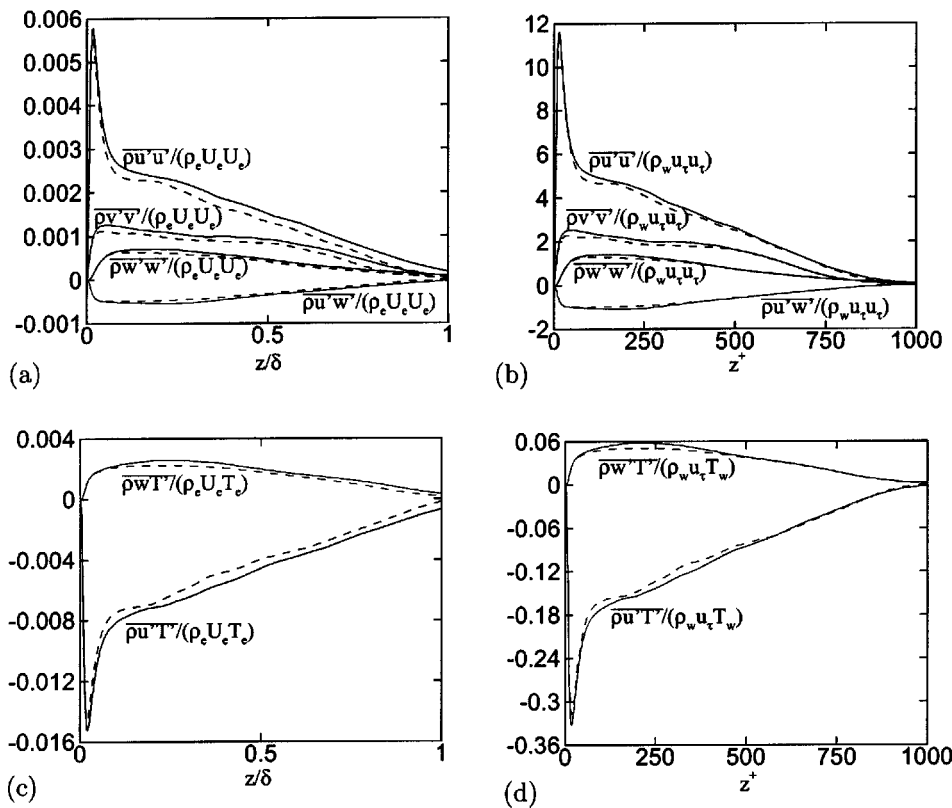
FIG. 9. Comparison between TDNS and ETDNS for (a)–(b) Reynolds stresses, (c)–(d) Reynolds heat fluxes. Quantities in (a) and (c) are nondimensionalized by the free stream parameters. Quantities in (b) and (d) are nondimensionalized by the wall parameters ETDNS: — and TDNS: ---.

the boundary later growth time. The total sampling time for the current TDNS is about 3 ($\delta_0^*/u_{\tau 0}$). The boundary layer in TDNS can be considered quasisteady if the flow adjusts to its local conditions much faster than the boundary layer growth. The adjusting time is of the order of the large-eddy-turn-over time δ_0/U_e, which is much smaller than the growth time. Thus, the conditions for the validity of TDNS are satisfied in the present simulation. Further comparisons between TDNS and ETDNS also validate the use of TDNS.

In ETDNS, the mean streamwise momentum balance is

$$\frac{\partial \langle \rho u \rangle}{\partial t} = -\frac{\partial \langle \rho u w \rangle}{\partial z} + \frac{\partial \langle \tau_{xz} \rangle}{\partial z} + \langle f_u \rangle, \tag{43}$$

where the terms at the right-hand side represent advection, diffusion, and forcing. Figure 7 shows these terms normalized with the freestream momentum $\rho_e U_e$ and the large-eddy turn-over time δ/U_e. From Fig. 7 we see that the time derivative of the mean streamwise momentum remains small in the boundary layer, with a maximum magnitude of less than 0.5%. Figure 7 also shows that the advection and diffusion are dominant in the viscous sublayer and they nearly balance each other. Outside the viscous sublayer, the diffusion is very small, in turn the forcing and advection terms balance each other.

The profiles of the mean streamwise velocity and the mean temperature are compared in Fig. 8(a). A mean quantity here is obtained by averaging in both space and time. The difference between TDNS and ETDNS is small for each of these quantities. Figure 8(b) plots the mean temperature vs the mean streamwise velocity and compare the resulting profiles with the one by Walz's equation. It can be seen that

Walz's equation predicts very well the relationship between the mean streamwise velocity and the mean temperature for the conditions chosen, and it can be used instead in the rescaling method for zero-pressure-gradient supersonic turbulent boundary layers.

2. Turbulence statistics

The Reynolds stresses and the Reynolds heat fluxes are compared between TDNS and ETDNS in Fig. 9. Primes are used to denote fluctuations with respect to the Reynolds-averaged mean. Due to the statistical symmetry in the spanwise direction, the Reynolds shear stresses $\overline{\rho u' v'}$ and $\overline{\rho v' w'}$ and the Reynolds heat flux $\overline{\rho v' T'}$ converge to zero, and they are not shown in Fig. 9. To observe the different temporal behavior of these quantities, we nondimensionalize them by the freestream parameters, i.e., ρ_e, U_e, and T_e. As seen in Fig. 9, the magnitude of each Reynolds stress component in TDNS is slightly smaller than the corresponding one in ETDNS. The statistics resulting from long-time-averaging a slowly decaying flow would have smaller amplitude than those of ETDNS. This is why the magnitudes of the TDNS statistics are slightly smaller than those for the ETDNS in Fig. 9. However, the difference is very small, and we consider the agreement to be good enough to draw our conclusion of the validity of TDNS. Scaled with wall parameters, i.e., ρ_w, u_τ, and T_τ ($T_\tau = T_w$ for an adiabatic wall and $T_\tau := P_{rw} q_w / \rho_w C_{pw} u_\tau$ for an isothermal wall, where P_{rw} is the Prandtl number and q_w the heat diffusion flux at the wall), we can still observe the similar difference for these quantities, which may indicate that the turbulence in TDNS evolves

2634   Phys. Fluids, Vol. 16, No. 7, July 2004
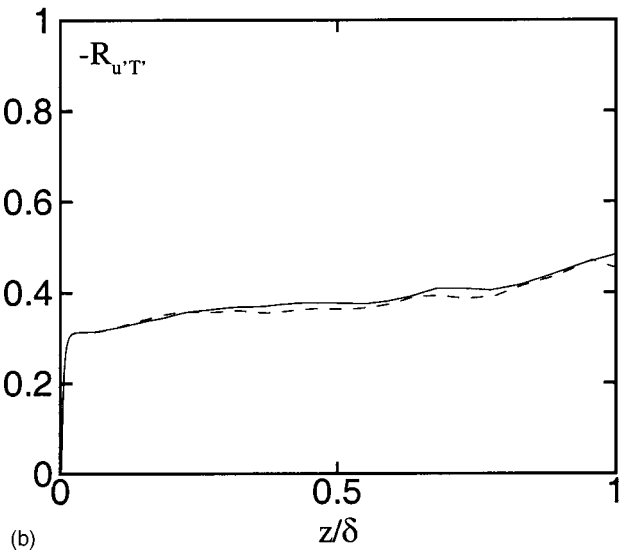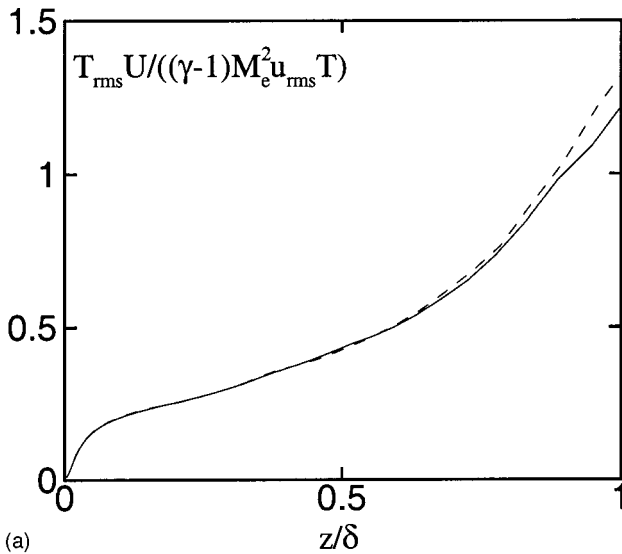
S. Xu and M. P. Martin

(a)

(b)

FIG. 10. (a) Amplitude and (b) phase relationship between temperature fluctuations and streamwise velocity fluctuations. ETDNS: — and TDNS: ---.

in a non-self-similar way. The same phenomena are also found for root mean squared fluctuating velocities, temperature and total temperature. Nevertheless, the difference in the current and later comparisons between TDNS and ETDNS is very small, which means the use of TDNS is valid.

The SRA predicts the relation between the temperature fluctuations and the streamwise velocity fluctuations as in Eq. (30). From the SRA, we know $T_{rms}U/(\gamma-1)M_e^2 T u_{rms} = 1$ and $-R_{u'T'} = 1$. Figure 10 plots $T_{rms}U/(\gamma-1)M_e^2 T u_{rms}$ and $-R_{u'T'}$ vs z/δ and indicates that the SRA is not satisfied in the bulk of the boundary layer simulated by both TDNS and ETDNS.

After assuming homogeneity of turbulence in the streamwise and spanwise directions, the turbulent kinetic energy (TKE) budget equation reads

$$\frac{\partial}{\partial t}(\langle\rho\rangle\tilde{k}) + \tilde{w}\frac{\partial}{\partial z}(\langle\rho\rangle\tilde{k}) = \mathcal{P} + \mathcal{T} + \Pi_t + \Pi_d + \mathcal{D} - \Phi + \mathcal{V}_c,$$
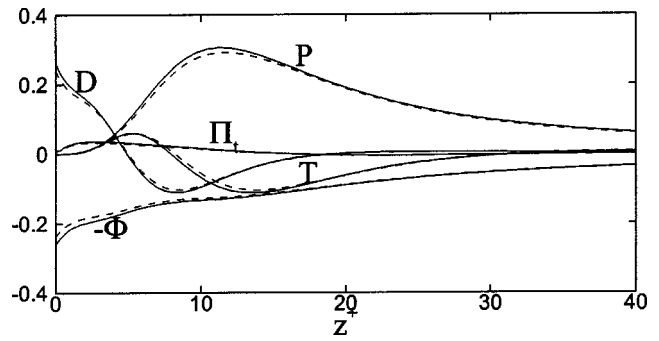
$$(44)$$

FIG. 11. Comparison of the TKE budget in TDNS and ETDNS. ETDNS: — and TDNS: ---.

where a quantity with a tilde is a mass-averaged mean. The terms in Eq. (44) follow the usual interpretations. Figure 11 gives the comparison of the TKE budget nondimensionalized by wall parameters between TDNS and ETDNS. Again, a small difference exists and the reason for the difference is the same as in Fig. 9.

B. SDNS

The rescaling method results in a spatial boundary layer. Figure 12 shows the spatial evolution of the boundary layer displacement thickness δ^*, momentum thickness θ, friction velocity u_τ and friction coefficient C_f. The rescaling method builds up the spatial boundary layer from the initial periodic flow field after the temporal transient is passed. The solid circles represent the time-averaged spatial distributions of these quantities for the spatial boundary layer in equilibrium. The time average period is $1.1\delta_0/u_{\tau 0}$. As seen from Fig. 13, the specified inlet friction velocity is about 8% larger than the mean friction velocity of the initial flow field while the momentum thickness is the same, which makes the described trick (Sec. III D) necessary to avoid a jump start. Figure 13 shows the spatial evolution of the shape factor, H, in comparison with Coles empirical correlation[36] and experimental data.[37] For this figure only, δ^* and θ are computed using the incompressible formulas and $Re_{\delta 2} = \rho_\delta u_\delta \theta/\mu_w$, where μ_w is the viscosity at the wall. Figure 13 shows that the SDNS data are within the experimental uncertainty. Experiments show that the shape factor is not constant, especially at low Reynolds numbers.[30] The accuracy of the shape factor decay is difficult to assess given the small range of $Re_{\delta 2}$ that we considered.

There are no experimental results at the present conditions, however, the maximum error based on the van Driest II theory in the skin friction is 7% for the SDNS data, as we show below. Hopkins and Inouye[23] presented a survey comparing different theories to predict the turbulent skin friction in supersonic and hypersonic boundary layers. They found that the van Driest II theory gives the best prediction. This prediction is widely accepted by experimentalists in supersonics and hypersonics. Below, we summarize this theory and show that the SDNS data is in very good agreement with this well-established theory.

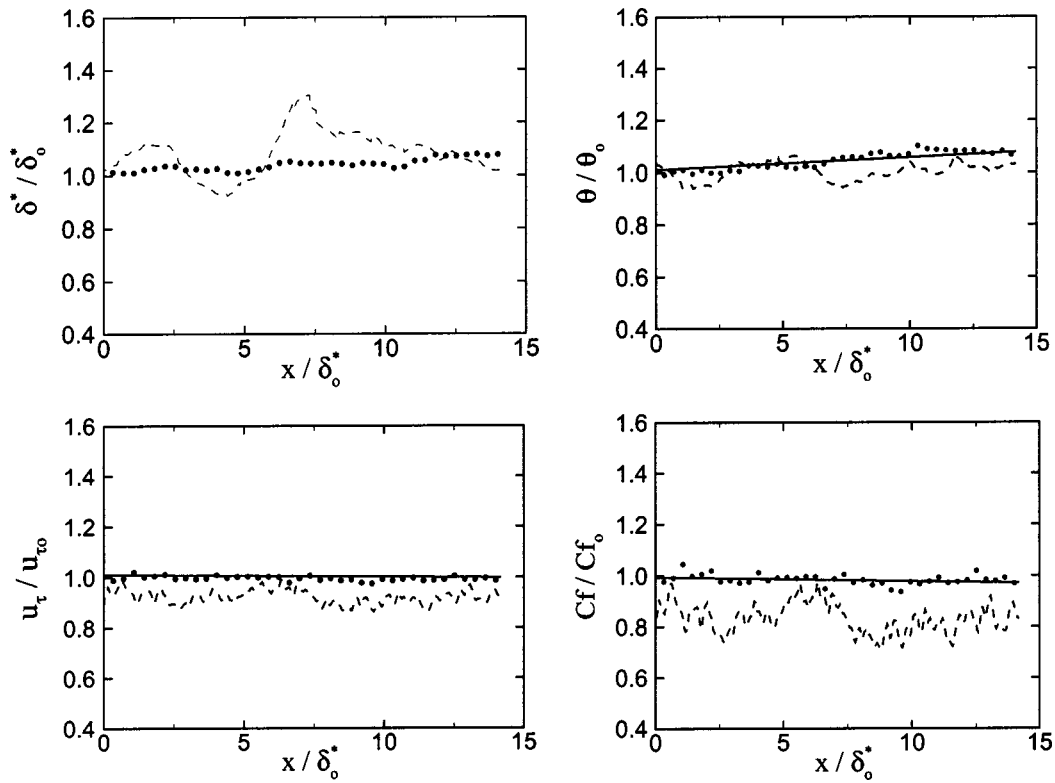Sivells and Payne formula[23] under van Driest II transformation reads

FIG. 12. Distributions of the displacement thickness δ^*, momentum thickness θ, friction velocity u_τ, and friction coefficient C_f along the streamwise direction. SDNS: ●; initial periodic flow field: ---; and formulas from least square (LS) minimization: —. The variables are nondimensionalized by the initial ones for the SDNS.

$$F_c C_f = \frac{0.088[\lg(F_x \operatorname{Re}_x) - 2.3686]}{[\lg(F_x \operatorname{Re}_x) - 1.5]^3}, \tag{45}$$

$$F_\theta \operatorname{Re}_\theta = \frac{0.044 F_x \operatorname{Re}_x}{[\lg(F_x \operatorname{Re}_x) - 1.5]^2}, \tag{46}$$
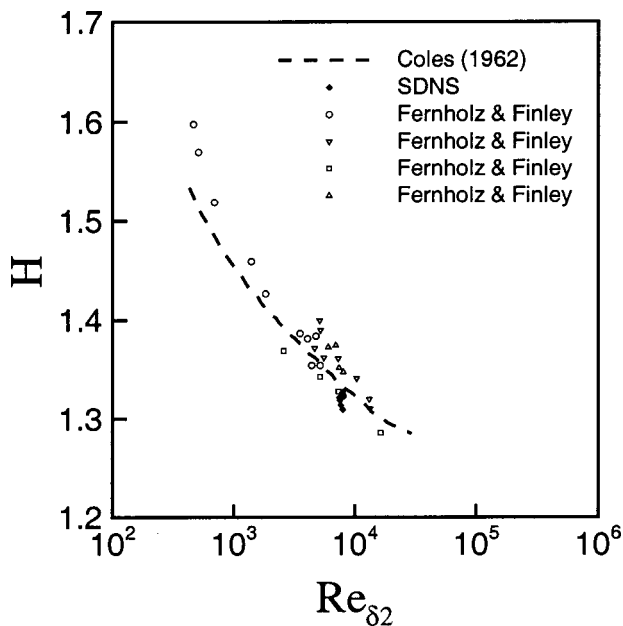
FIG. 13. Variation of shape factor H with Reynolds number in comparison with experimental data (Ref. 12) and the empirical correlation of Coles (Ref. 6). Here, the variables are computed using the incompressible formulas.

where C_f is the local skin friction coefficient, Re_x ($= \rho_e U_e x / \mu_e$) is Reynolds number based on distance to the virtual origin of the boundary layer, Re_θ is Reynolds number based on the momentum thickness as defined in Table I. For a given Re_θ, we compute C_f from the estimation by Karman–Schoenherr equation under van Driest II transformation.[23] After C_f is calculated, we compute Re_x from Eq. (45). Karman–Schoenherr equation under van Driest II transformation reads

$$\frac{1}{F_c C_f} = 17.08[\lg(F_\theta \operatorname{Re}_\theta)]^2 + 25.11 \lg(F_\theta \operatorname{Re}_\theta) + 6.012. \tag{47}$$

F_c, F_θ, and F_x are van Driest II transformation functions computed as

$$F_c = \frac{0.2 r M_e^2}{(\sin^{-1} \alpha + \sin^{-1} \beta)^2}, \tag{48}$$

$$F_\theta = \frac{\mu_e}{\mu_w}, \tag{49}$$

$$F_x = \frac{F_\theta}{F_c}, \tag{50}$$

where r is recovery factor and α and β are calculated by

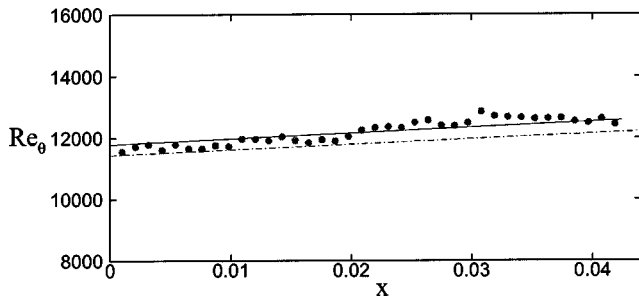$$\alpha = \frac{2A^2 - B}{\sqrt{4A^2 + B^2}}, \tag{51}$$

FIG. 14. Distribution of Re_θ along the streamwise direction. SDNS: ●; estimation by Eqs. (45) and (47): –·–; and formula from least square (LS) minimization: —.

$$\beta = \frac{B}{\sqrt{4A^2 + B^2}}, \tag{52}$$

with

$$A = \sqrt{\frac{0.2rM_e^2}{F}}, \tag{53}$$

$$B = \frac{1 + 0.2rM_e^2 - F}{F}, \tag{54}$$

$$F = \frac{T_w}{T_e}. \tag{55}$$

Figure 14 shows that the streamwise evolution of Re_θ from the simulation is in excellent agreement with that one given by Eqs. (45) and (47). Knowing u_τ, we calculate Re_x at the inlet from Eq. (45) and obtain data correspondence in SDNS between Re_θ and Re_x. We then use the least square (LS) minimization to produce a formula similar to Eq. (46). The solid line in Fig. 14 represents the plot from the LS minimization. Its slope matches very well the slope estimated by Eq. (46). For comparison, we have shifted the virtual origin of the boundary layer to the boundary layer inlet. The relative magnitude difference between the LS results and the predictions given by Eq. (46) is less than 2% for the LS fitted data (less than 5% for the data without LS fit). In Fig. 12, the LS results for θ distribution are given by a solid line.

Figure 15 compares the simulated local skin friction C_f in terms of Re_θ with the estimation by Eq. (47). The dashed–dotted line represents the estimation, solid circles denote
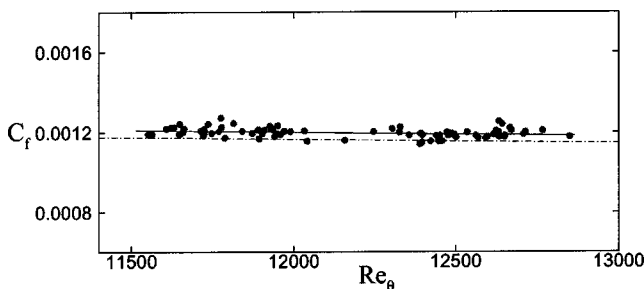

FIG. 15. Distribution of the local skin friction C_f in terms of Re_θ. SDNS: ●; Eq. (47): –·–; and formula from LS minimization: —.
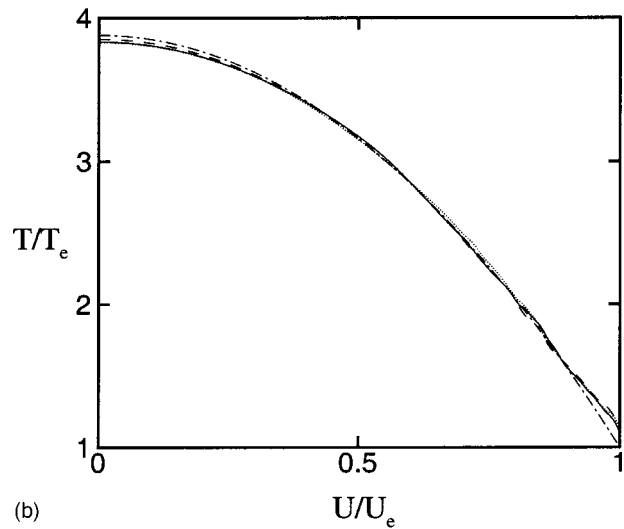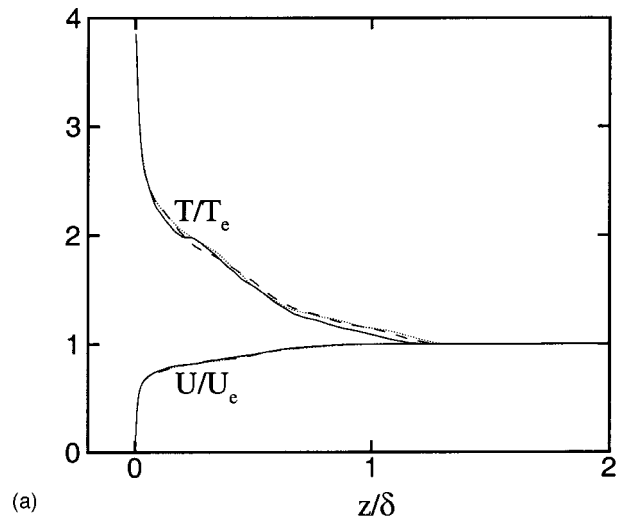

(a)

(b)

FIG. 16. Mean streamwise velocity and temperature (a) distributions, (b) comparison with Walz's equation for $r = 0.9$. Station 1: –·–; Station 2: ---; Station 3: —; and Walz's equation: –·–.

time-averaged values from the spatial simulation. The solid line represents the results of the LS minimization which uses SDNS data to produce a formula similar to Eq. (47). We observe that the result from the simulation is in good agreement with the estimation. The relative magnitude difference between the LS results and the predictions given by Eq. (47) is about 3.3% for the LS fitted data (less than 7% for the data without LS fit).

Figure 16(a) shows the mean streamwise velocity and the mean temperature, scaled by the freestream parameters, at three different streamwise stations marked as (1), (2), and (3) in Fig. 4 which, respectively, correspond to $x_1 = 0.3\delta_0$, $x_2 = 2.4\delta_0$, and $x_3 = 4.5\delta_0$. Because the evolution of the mean flow is very small due to the small streamwise extent, little difference is observed. Figure 16(b) plots the relationship between the mean streamwise velocity and the mean temperature at these stations. It can be seen that the relationship is independent of the streamwise location, which verifies the assumption that we made in the rescaling method.
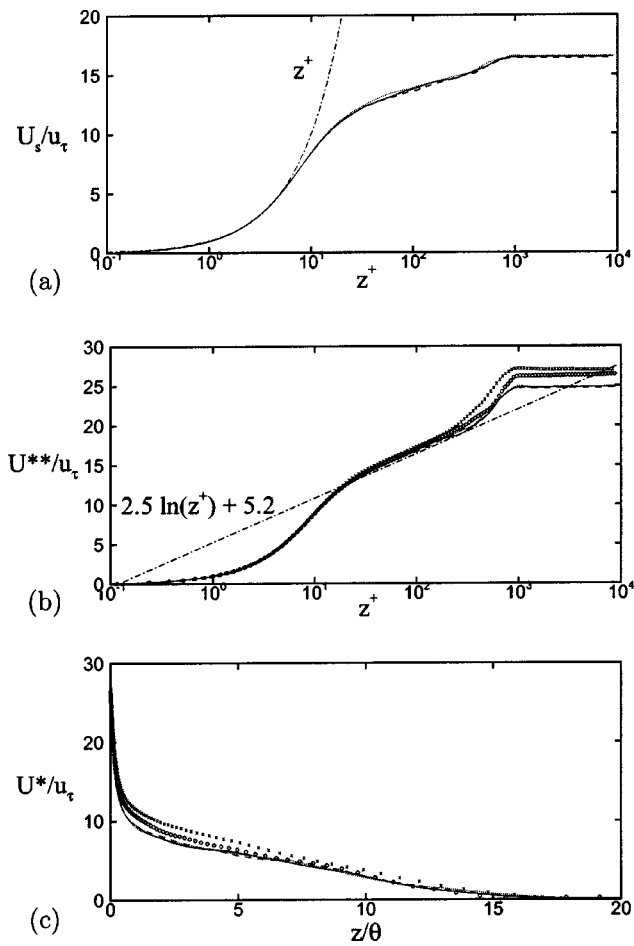
FIG. 17. Transformed mean streamwise velocity using (a) Eq. (8), (b) Eq. (14) and (c) Eq. (18). Station 1: $-\cdot-$; Station 2: ---; Station 3: —; TDNS station: $\times$; and the fourth station of ETDNS: $\bigcirc$.

For this zero-pressure-gradient boundary layer, Walz's equation can describe the relationship very well.

Figure 17(a) shows the mean streamwise velocity profiles under the transformation given by Eq. (8) at the three stations. The transformed velocity is scaled by u_τ, and the wall-normal coordinate is nondimensionalized by the wall units. Figure 17(a) shows that the profiles collapse very well using the transformation and scaling in the viscous region ($z+ < 5$), and they satisfy the theoretical linear relationship in the viscous region. Figure 17(b) shows the van Driest transformed mean streamwise velocity profiles scaled with u_τ at the three stations. Results from TDNS and ETDNS are also included. The wall-normal coordinate is also nondimensionalized using wall units. Figure 17(b) shows that the profiles collapse very well using the transformation and scaling in the logarithmic region ($30 < z^+ < 200$ in our case), and they satisfy the theoretical logarithmic law. Near the boundary layer edge, the mean streamwise velocity profiles from SDNS, TDNS, and ETDNS do not collapse using the above transformation. However, Fig. 17(c) shows that the data collapse when we use the transformation given by Eq. (18) with the wall coordinate scaled by the momentum thickness. In fact, Eq. (18) gives the van Driest transformation on the mean streamwise velocity defect.

Figure 18 shows the profiles of Reynolds stresses and Reynolds heat fluxes at the three stations. They are obtained by averaging scaled Reynolds stresses and Reynolds heat fluxes in time. The wiggles on the profiles are due to the insufficiency of averaging samples. In Figs. 18(a) and 18(c), the freestream parameters are to nondimensionalize the variables. In Figs. 18(b) and 18(d), the wall parameters are used instead. We may expect that the spatial evolution of a Reynolds stress or a Reynolds heat flux from Station 1 to Station
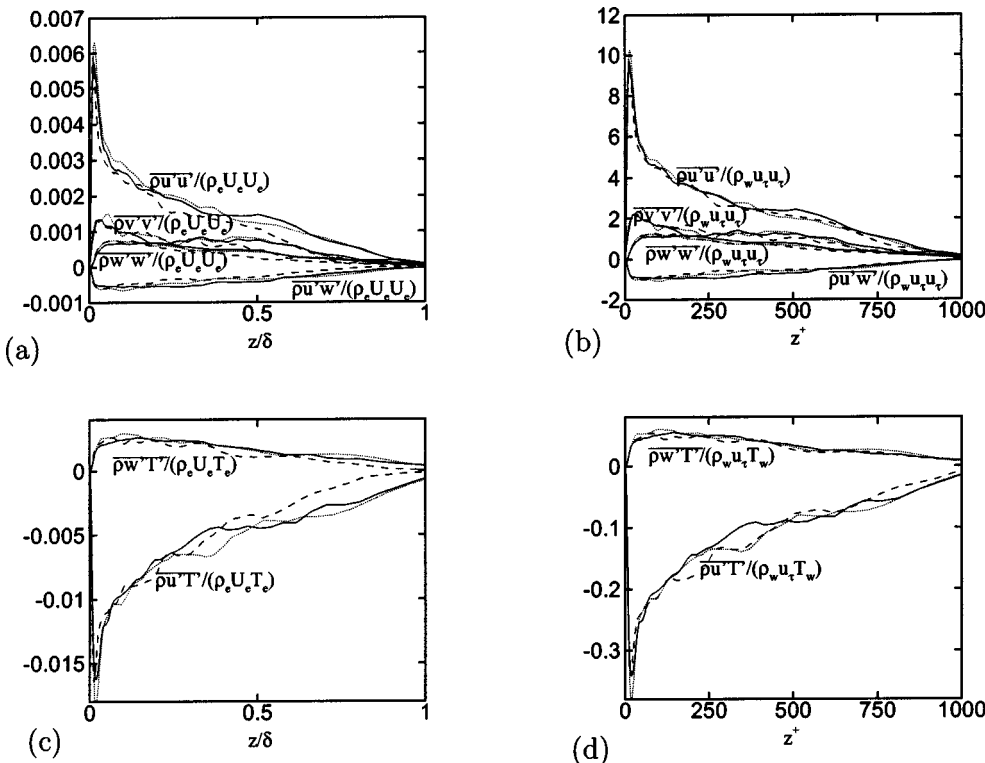

FIG. 18. Comparisons among Stations 1, 2, and 3 for (a)–(b) Reynolds stresses, (c)–(d) Reynolds heat fluxes. Quantities in (a) and (c) are nondimensionalized by the free stream parameters. Quantities in (b) and (d) are nondimensionalized by the wall parameters. Station (1): $-\cdot-$; Station (2): ---; Station (3): —.
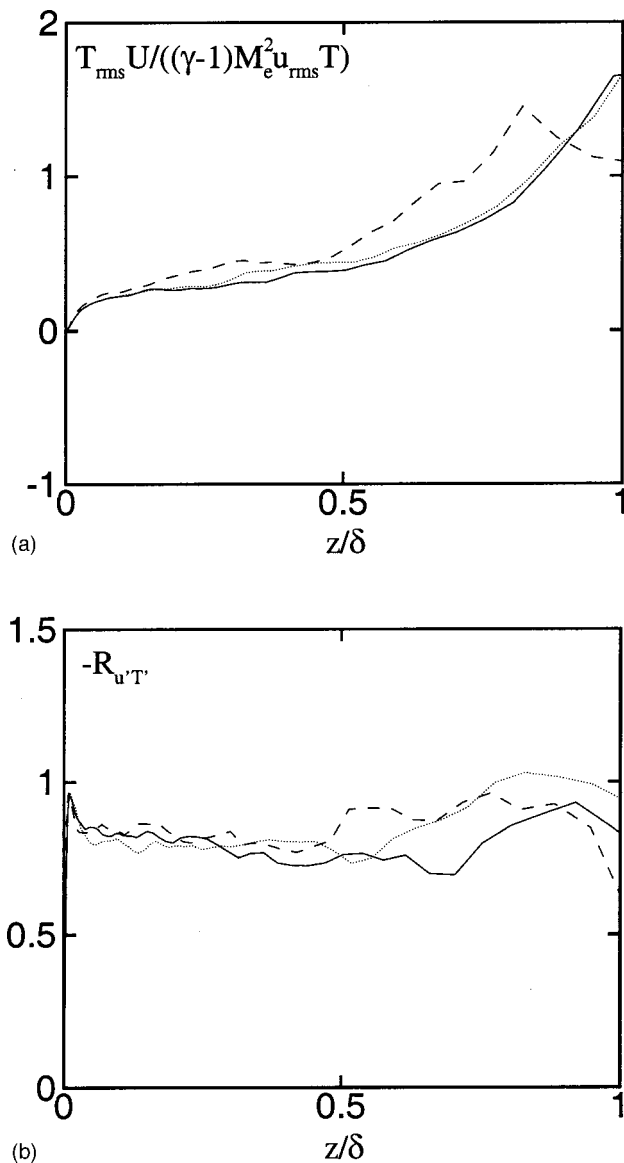
FIG. 19. Plots of the (a) amplitude and (b) phase relationships between the temperature fluctuations and the streamwise velocity fluctuations. Station (1): $-\cdot-$; Station (2): $---$; Station (3): $—$.

and decaying turbulence. However, the usage is valid provided that the turbulence is quasisteady and sustains for sufficient time to gather statistics without apparent boundary layer growth. We find that good quasistationary flow statistics can be obtained if the sampling time is one order of magnitude smaller than the characteristic flow-evolution time. The extended temporal approach adds forcing to the governing equations to account for the streamwise inhomogeneity and can achieve a statistically stationary mean flow and turbulence. The forcing is constructed from available information of flow evolution and no *a priori* assumptions about the flow are needed. The marching process in the extended approach allows the simulation of a series of boundary layer stations. The data from the simulations with genuine periodic boundary conditions are in good agreement with those obtained from the extended temporal simulations, which shows the validity of the use of genuine periodic boundary conditions.

The rescaling method proposed in this paper is designed for the spatial simulation of compressible turbulent boundary layers. The main assumptions behind the method are that the compressibility effects reduce to density variation effects and that general temperature–velocity relationships exist in the boundary layer. Based on similarity laws, the method rescales the flow field at a recycling station and then reintroduces the rescaled flow field to the inlet. The data show that the method results in a spatial simulation which generates its own inflow with little transient adjustment behind the inlet. The simulation is carried out over a zero-pressure-gradient flat plate, but the method may be extended to cases with pressure gradient and/or geometric change because the method does not assume any specific forms of similarity laws and temperature–velocity relationships. As pointed out by Lund *et al.*[5] in their modified Spalart method, when the inlet is under a pressure distribution in equilibrium, the required changes in their method as well as ours involve only the computation of the friction velocity at the inlet and the vertical velocity distribution at the upper boundary. The test simulation shows good agreement with the theory.

Realistic turbulence inflow is desired for a boundary layer simulation, but it is not achievable unless a forced transition is used, which can be very costly for controlled boundary layer conditions. The proposed rescaling technique is a good alternative in terms of accuracy and efficiency. We should also mention that under certain conditions, air reactions take place in the boundary layer.[28,38] Currently, there are no rescaling techniques to approximate the inflow. Thus, understanding under what limiting conditions TDNS can be considered is useful.

3 is small because the three stations are close. However, Figs. 18(a) and 18(c) show that the difference among the three stations is quite apparent. This may originate from insufficiency averaging samples. When scaled by wall parameters, the difference becomes much smaller, as indicated by Figs. 18(b) and 18(d).

Figure 19 plots $T_{\text{rms}}U/(\gamma-1)M_e^2 T u_{\text{rms}}$ and $-R_{u'T'}$ vs z/δ at the three stations. In Fig. 19, we observe that assuming a streamwise-location-independent relation between the temperature fluctuations and the streamwise velocity fluctuations, as in Eq. (32), is a good assumption. The rigorous SRA is not satisfied in the bulk of the boundary layer.

V. CONCLUSIONS

The use of genuine periodic boundary conditions in a temporal simulation neglects the streamwise inhomogeneity of the boundary layer and thus results in evolving mean flow

ACKNOWLEDGMENTS

[1]C. L. Streett and M. G. Macaraeg, "Spectral multidomain for large-scale fluid dynamic simulations," Appl. Numer. Math. **6**, 123 (1989).

[2]N. A. Adams, "Direct numerical simulation of turbulent compression ramp flow," Theor. Comput. Fluid Dyn. **12**, 109 (1998).

[3]Y. Guo, N. A. Adams, and L. Kleiser, "A comparison study of an improved temporal DNS and spatial DNS of compressible boundary layer transition," AIAA J. **34**, 683 (1996).

[4]P. R. Spalart and J. H. Watmuff, "Experimental and numerical study of a turbulent boundary layer with pressure gradients," J. Fluid Mech. **249**, 337 (1993).

[5]T. S. Lund, X. Wu, and K. D. Squires, "Generation of turbulent inflow data for spatially-developing boundary layer simulations," J. Comput. Phys. **140**, 233 (1998).

[6]T. Maeder, N. A. Adams, and L. Kleiser, "Direct simulation of turbulent supersonic boundary layers by an extended temporal approach," J. Fluid Mech. **429**, 187 (2001).

[7]P. R. Spalart, "Direct simulation of a turbulent boundary layer up to Re_θ =1410," J. Fluid Mech. **187**, 61 (1988).

[8]P. R. Spalart and K. Yang, "Numerical study of ribbon-induced transition in Blasius flow," J. Fluid Mech. **178**, 345 (1987).

[9]N. Li and U. Piomelli, "Inflow conditions for large-eddy simulations of mixing layers," Phys. Fluids **12**, 935 (2000).

[10]N. A. Adams, "Direct simulation of the turbulent boundary layer along a compression ramp at $M=3$ and $Re_\theta=1685$," J. Fluid Mech. **420**, 47 (2000).

[11]D. P. Rizzetta, M. R. Visbal, and D. V. Gaitonde, "Large-eddy simulation of supersonic compression-ramp flow by high-order method," AIAA J. **39**, 2283 (2001).

[12]D. P. Rizzetta and M. R. Visbal, "Application of large-eddy simulation of supersonic compression ramps," AIAA J. **40**, 1574 (2002).

[13]Y. F. Yao, T. G. Thomas, N. D. Sandham, and J. J. R. Williams, "Direct numerical simulation of turbulent flow over a rectangular trailing edge," Theor. Comput. Fluid Dyn. **14**, 337 (2001).

[14]S. Lee, S. K. Lele, and P. Moin, "Simulation of spatially evolving turbulence and the applicability of Taylor's hypothesis in compressible flow," Phys. Fluids A **4**, 1521 (1992).

[15]M. M. Rai and P. Moin, "Direct numerical simulation of transition and turbulence in a spatially evolving boundary layer," J. Comput. Phys. **109**, 169 (1993).

[16]H. Le, P. Moin, and J. Kim, "Direct numerical simulation of turbulent flow over a backward-facing step," Report No. TF-58, Thermosciences Division, Department of Mechanical Engineering, Stanford University, 1994.

[17]M. Klein, A. Sadiki, and J. Janicka, "A digital filter based generation of inflow data for spatially developing direct numerical or large eddy simulations," J. Comput. Phys. **186**, 652 (2003).

[18]K. Bhaganagar, D. Rempfer, and J. Lumley, "Direct numerical simulation of spatial transition to turbulence using fourth-order vertical velocity second-order vertical vorticity formulation," J. Comput. Phys. **180**, 200 (2002).

[19]N. A. Adams and L. Kleiser, "Numerical simulation of transition in a compressible flat plate boundary layer," ASME: Transitional and Turbulent Compressible Flows, **151**, 101 (1993).

[20]H. Fasel and U. Konzelmann, "Nonparallel stability of a flat-plate boundary layer using the complete Navier–Stokes equations," J. Fluid Mech. **221**, 311 (1990).

[21]F. Ducros, P. Comte, and M. Lesieur, "Large-eddy simulation of transition to turbulence in a boundary layer developing spatially over a flat plate," J. Fluid Mech. **326**, 1 (1996).

[22]C. D. Pruett and C. L. Chang, "Direct numerical simulation of hypersonic boundary-layer flow over a flared cone," Theor. Comput. Fluid Dyn. **11**, 49 (1998).

[23]E. J. Hopkins and M. Inouye, "An evaluation of theories for predicting turbulent skin friction and heat transfer on flat plates at supersonic and hypersonic Mach numbers," AIAA J. **9**, 993 (1971).

[24]S. Stolz and N. A. Adams, "Large-eddy simulation of high-Reynolds-number supersonic boundary layers using the approximate deconvolution model and a rescaling and recycling technique," Phys. Fluids **15**, 2398 (2003).

[25]G. Urbin and D. Knight, "Large-eddy simulation of a supersonic boundary layer using an unstructured grid," AIAA J. **39**, 1288 (2001).

[26]L. Kleiser and T. A. Zang, "Numerical simulation of transition in wall-bounded shear flows," Annu. Rev. Fluid Mech. **23**, 495 (1991).

[27]S. E. Guarini, R. D. Moser, K. Shariff, and A. Wray, "Direct numerical simulation of a supersonic turbulent boundary layer at Mach 2.5," J. Fluid Mech. **414**, 1 (2000).

[28]M. P. Martin, "Preliminary DNS database of hypersonic turbulent boundary layers," AIAA Paper No. 03-3726, 2003.

[29]P. Bradshaw, "Compressible turbulent shear layers," Annu. Rev. Fluid Mech. **9**, 33 (1977).

[30]A. J. Smits and J. Dussauge, "Boundary layer mean-flow behavior," in *Turbulent Shear Layers in Supersonic Flows* (AIP, New York, 1996), p. 161.

[31]J. Gaviglio, "Reynolds analogies and experimental study of heat transfer in the supersonic boundary layer," Int. J. Heat Mass Transfer **30**, 911 (1987).

[32]J. F. Debiève, "Ètude d'une interaction turbulence/onde de choc," thèse de Dotorat d'État, Université d'Aix-Marseille II, 1983.

[33]J. P. Dussauge, "Évolution de transferts turbulents dans une détente rapide, en écoulement supersonique," thèse de Doctorat d'État, Université d'Aix Marseille, 1981.

[34]L. Fulachier, "Contribution à l'étude des analogies des champs dynamiques et thermiques dans une couche limite turbulente. Effet de l'aspiration," thèse de Doctorat ès Sciences Physiques, Université de Provence, Aix-Marseille, 1972.

[35]M. Israeli and S. A. Orszag, "Approximation of radiation boundary conditions," J. Comput. Phys. **41**, 115 (1981).

[36]D. Coles, "The turbulent boundary layer in a compressible fluid," Report No. R-403-PR, The Rand Corporation, Santa Monica, California, 1962.

[37]H. H. Fernholz and P. J. Finley, "Incompressible zero-pressure-gradient turbulent boundary layers: An assessment of the data," Prog. Aerosp. Sci. **32**, 245 (1996).

[38]M. P. Martin and G. V. Candler, "Temperature fluctuation scaling in reacting turbulent boundary layers," AIAA Paper No. 01-2717, 2001.

[39]C. C. Lin, "On Taylor's hypothesis and the acceleration terms in the Navier–Stokes equations," Q. Appl. Math. **10**, 295 (1953).